

# Impedance detection of the electrical resistivity of the wound tissue around deep brain stimulation electrodes permits registration of the encapsulation process in a rat model

Kathrin Badstübner<sup>1</sup>, Marco Stubbe<sup>2</sup>, Thomas Kröger<sup>3</sup>, Eilhard Mix<sup>1</sup>, and Jan Gimsa<sup>2,4</sup>

1. Department of Neurology, University of Rostock, Rostock, Germany
2. Chair of Biophysics, University of Rostock, Rostock, Germany
3. Chemical Institute, University of Rostock, Rostock, Germany
4. E-mail any correspondence to: [jan.gimsa@uni-rostock.de](mailto:jan.gimsa@uni-rostock.de)

## Abstract

An animal model of deep brain stimulation (DBS) was used in *in vivo* studies of the encapsulation process of custom-made platinum/iridium microelectrodes in the subthalamic nucleus of hemiparkinsonian rats via electrical impedance spectroscopy. Two electrode types with 100- $\mu\text{m}$  bared tips were used: i) a unipolar electrode with a 200- $\mu\text{m}$  diameter and a subcutaneous gold wire counter electrode and ii) a bipolar electrode with two parallel-shifted 125- $\mu\text{m}$  wires. Miniaturized current-controlled pulse generators (130 Hz, 200  $\mu\text{A}$ , 60  $\mu\text{s}$ ) enabled chronic DBS of the freely moving animals. A phenomenological electrical model enabled recalculation of the resistivity of the wound tissue around the electrodes from daily *in vivo* recordings of the electrode impedance over two weeks. In contrast to the commonly used 1 kHz impedance, the resistivity is independent of frequency, electrode properties, and current density. It represents the ionic DC properties of the tissue. Significant resistivity changes were detected with a characteristic decrease at approximately the 2nd day after implantation. The maximum resistivity was reached before electrical stimulation was initiated on the 8th day, which resulted in a decrease in resistivity. Compared with the unipolar electrodes, the bipolar electrodes exhibited an increased sensitivity for the tissue resistivity.

**Keywords:** wound healing detection; intracerebral electrodes; neuronal interface; electrode impedance; cell constant; constant phase element

## Introduction

Neuromodulation is among the fastest growing areas in medicine. It involves cortical and sub-cortical electrical stimulation for the treatment of an increasing number of neurological and psychiatric diseases. Among interventions that use electrical stimulation to treat movement disorders, such as Parkinson's disease (PD), deep brain stimulation (DBS) is probably the most successful approach [1]. High-frequency (approx. 130 Hz, 60- $\mu\text{s}$  needle pulses) DBS of the subthalamic nucleus (STN) is an effective therapeutic option for PD patients, particularly in the advanced stages of the disease, who are refractory to conventional therapy [2, 3]. However, the clinical DBS therapies may have not reached optimal efficiency. For example, the best target regions are not clear and the basic mechanisms of action remain poorly understood [4]. This situation results in a striking contrast between the boom of the clinical applications and a relatively poor knowledge in basic research. One reason for this contrast is the insufficient availability of chronic stimulation devices for small laboratory animals. In practice, there is a need for research in two fields, the optimization of DBS equipment and the exploration of the physiological DBS mechanisms. The first field of research requires the miniaturization of stimulation devices and the development of DBS electrodes, counter-electrodes and implantation techniques for animals, whereas the second field aims to

optimize the stimulation parameters and brain regions in the animal model.

Clinical DBS devices commonly use constant-voltage stimulation, whereas constant-current stimulation guarantees constant field strengths and stimulation efficiency in the surrounding tissue of small animal electrodes by circumventing the effects of impedance alterations at the electrode interface or in the capsule (adventitia) tissue [5]. Studies have demonstrated that current-controlled devices may also improve the therapeutic effects in patients [6-9].

To date, most published DBS experiments with animal models use short-term (acute) stimulation, in some cases only in anaesthetized animals, directly after electrode implantation. In these experiments, external stimulators are often used, and the behavioral outcomes are not examined [10-15]. In another approach, implanted DBS electrodes are connected to stationary stimulators via cables, which enable the movement of the animals in a confined area during behavioral testing [16-18]. DBS stimulators fixed to the heads of rats enabled the animals to move freely in experiments conducted for up to five weeks [19, 20].

As an alternative, relatively large stimulators were implanted at the expense of an invasive surgery [21]. Here, we use chronic DBS in a rat model under spontaneous movement conditions. Our approach combines a miniaturized stimulator and batteries in a textile backpack with custom-made DBS electrodes, which are connected via subcutaneous wires. Our chronic instrumentation [22] aims to prolong the observation periods up to six weeks, which represents a challenge that has been met only in a limited number of publications [23; for detailed reviews see: 24, 25].

In previous studies, we focused on the identification of optimal DBS electrode materials, geometries and stimulation currents under the aspects of biocompatibility and stimulation efficiency. Starting from basic *in vitro* studies [26] and numerical considerations [5], animal experiments [for detailed review see: 27] were conducted using the hemiparkinsonian rat model [28]. These investigations have demonstrated that the use of commercial stainless steel electrodes should be avoided because of corrosion and erosion processes, which are intensified by the electrolytic electrode processes. The problem may be reduced by appropriate electrode materials. Electrochemically, platinum/iridium (Pt/Ir) electrodes are substantially more stable, even though electrochemical byproducts of electrode processes may influence the surrounding tissue.

Electrical impedance spectroscopy is a common, non-destructive technique for determining the electrical

properties of tissues [29]. It is used in a wide range of medical applications, such as breast-cancer detection [30], lung volume monitoring [31], and heart ischemia during surgery [32]. Impedance spectroscopy is also suitable for the characterization of DBS electrodes [26] and the encapsulation process of DBS electrodes [33, 34]. After implantation, the impedances of DBS [35] or cochlear electrodes [36, 37] tend to increase. Typically, the foreign body reaction in rats and, in turn, the electrode impedance stabilize after several weeks [38]. This stabilization process has been demonstrated to be perturbed by electrical stimulation in DBS [39] and intra-cochlear electrodes [37, 40]. For an optimal adjustment of DBS signals, the kinetics of the resulting electrode-impedance changes by the adventitia formation must be taken into account [41].

Here, we present *in vivo* studies of the encapsulation process of custom-made unipolar and bipolar Pt/Ir microelectrodes in the subthalamic nucleus of freely moving rats for one week after surgery and under chronic DBS for a second week. Impedance spectroscopy was used to follow the resistivity (in  $\Omega\text{m}$ ), i.e., the reciprocal specific conductivity (in S/m) around the implanted electrodes. The resistivity was extracted from the impedance spectra using a new way of data interpretation. We suggest that the obtained resistivities are a measure for the balance of the media that surrounds the electrode, such as the free interstitial (wound) fluid, adventitia, and neuronal tissue. Resistivity changes are caused by the foreign body reaction, i.e., adventitia encapsulation, as well as electrochemical processes driven by the stimulating current and the subsequent tissue response at the electrode surfaces.

## Materials and methods

### Electrodes

Microelectrodes were custom-made from round Pt/Ir alloy (Pt90/Ir10) wires, which were insulated with polyesterimide and bared at the tips (Figure 1). The microelectrodes were purchased from Polyfil, Zug, Switzerland (unipolar electrodes) and FHC, Bowdoin, ME, USA (bipolar electrodes). Their distal ends were connected to cables with biocompatible insulation. To avoid excessive heating by soldering, the cables were connected with conductive silver glue, which was covered by biocompatible heat-shrink tubing and sealed with biocompatible silicon glue (NuSil Technology, Carpinteria, CA, USA). The unipolar electrodes were driven and measured against a gold-wire counter electrode (length 30 mm, diameter 200  $\mu\text{m}$ ). The bipolar electrodes did not require an additional counter electrode.

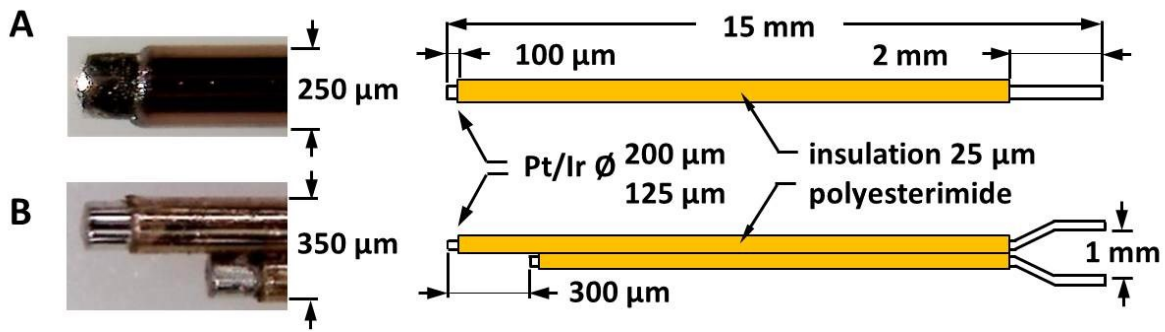


Figure 1: Photographs of tips (left) and schematic drawings (right) of (A) a unipolar electrode (200 μm wire diameter) and (B) a bipolar electrode (125 μm wire diameter). The electrode shafts were insulated with 25 μm polyesterimide. All electrode tips were bared for 100 μm.

### Electrical impedance spectroscopy

Control and animal measurements of the impedance were conducted using a Sciospec ISX3-spectrometer (Sciospec Scientific Instruments, Pausitz, Germany) with a HP16047D-test fixture (Agilent Technologies Deutschland GmbH, Böblingen, Germany). The DBS and counter-electrode wires were connected to the test fixture. The Sciospec measuring software was programmed to average over five measuring cycles at a measuring voltage of 12.5 mV<sub>pp</sub> in a frequency range from 100 Hz to 10 MHz. The real ( $Real(Z^*)$ ) and imaginary ( $Imag(Z^*)$ ) components of 401 frequency points were logged with a personal computer. The measuring frequencies were equidistant at a logarithmic frequency scale.

Prior to each measurement, the impedance spectrometer was open, short and load calibrated. Each measurement was repeated three times to improve the statistical validity. Finally, the logged data were transferred to Matlab (The MathWorks™, Version 7.9.0.529, Natick, MA, USA) for further processing. The impedance was measured within the frequency range from 100 Hz to 10 MHz for two reasons: i) the steep slopes of the needle-shaped stimulation pulse of the DBS signal are rich in high harmonic frequencies [26] and ii) complete impedance spectra were required for the extraction of the tissue resistivities (c.p. also to [33]).

### Electrode impedance: equivalent circuit and data interpretation

Control measurements of the impedance were conducted in beakers with a calibration solution that had a conductivity of  $\sigma_{cal}=0.1307 \text{ Sm}^{-1}$  (HI77100C, HANNA Instruments Deutschland GmbH, Vöhringen, Germany). For measurements, the electrodes were immersed to approx. 90% of their shaft lengths. The gold-wire counter electrode was oriented approximately perpendicular to the shaft of the unipolar electrode (cf. Figure 3). Figure 2 provides a schematic summary and introduces the terms used in the description of the electrode impedance.

In the complex plane, the transition frequency from a linear (“constant phase”) to a semicircle shape indicates the cessation of electrode polarization processes. Their contributions to the overall impedance vanish for increasing frequencies, which renders the impedance to pure resistance and capacitance contributions of the wiring and bulk medium (or of the brain tissue) that surrounds the electrode [26]. For ideal electrodes and pure electrolytes, the parallel circuit of  $R_{Bulk}$  and  $C_{Bulk}$  would result in a perfect semicircle with its center at the abscissa. The transition frequency between the linear and semicircle branches depends on the electric medium and electrode-surface properties. The constant phase element (CPE) provides a phenomenological description of the frequency-dependent impedance contributions of the electrode processes and the double layer properties at the electrolytic interfaces (see equivalent circuit in Figure 6; [42, 43]). Electrotechnically speaking, the CPE may be considered a serial cascade of parallel resistor-capacitor pairs with consecutively increasing time constants [44].

When impedance data were recorded with zero bias voltage, special elements for the charge-transfer resistance and the double-layer capacitance may be neglected [26]. In this case, the CPE may be mathematically described by [45-47]:

$$Z_{CPE} = \frac{1}{Q(j\omega)^\alpha} \quad (1)$$

where  $\omega$  indicates the angular frequency  $2\pi f$  and  $j=\sqrt{-1}$ .  $Q$  is a constant with a dimension of  $Fs^{(\alpha-1)}$ . The exponent  $\alpha$ , with  $0 < \alpha < 1$ , describes the slope of the linear branch in the complex plot. The limiting cases  $\alpha=0$  and  $\alpha=1$  describe a purely resistive or capacitive impedance behavior, respectively. The straight lines in Figure 2A are described by equation (1), and the semicircles reflect the impedance properties of the parallel resistor-capacitor pair.

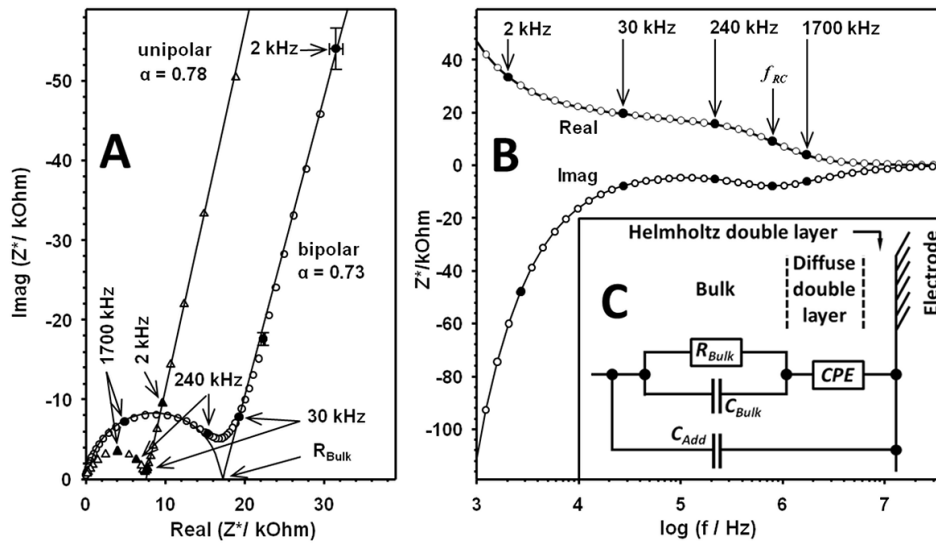


Figure 2: Illustration of the impedance  $Z^*$  of unipolar and bipolar electrodes measured in the calibration solution. For clarity, not all 401 measuring points per spectrum were plotted, and error bars are only provided as examples. Above 30 kHz, all error bars were smaller than the size of the measuring point symbols. (A) Complex plots illustrate the fitting procedure for  $R_{Bulk}$  using a straight line and a semicircle. For  $\alpha$ , see equation (1). The plots indicate that CPE effects are pronounced in a wider frequency range in the spectrum of the bipolar electrode compared with the unipolar electrode. Measuring points for 2, 30, 240, and 1700 kHz are filled. (B) Plot of the real and imaginary parts of the impedance of the bipolar electrode over the frequency. In (A), the characteristic frequency  $f_{RC}$  is located above the center of the semicircle. (C) Equivalent circuit of the electrode impedance and its surrounding medium.  $R_{Bulk}$  and  $C_{Bulk}$  describe the properties of the bulk medium in contact with the bared electrode contacts.  $C_{Add}$  summarizes additional capacitances in the measuring setup. The CPE describes the impedance of the electrode effects at the metal-medium interface. For the calibration solution,  $R_{Bulk} = R_{Cal}$ .

For a cubic measuring volume with bulk properties, confined by two plane-parallel electrodes of area  $a^2$  and distance  $a$ ,  $R_{Bulk}$  and  $C_{Bulk}$  are:

$$R_{Bulk} = \rho_{Bulk} \frac{a}{a^2} = \frac{\rho_{Cal}}{\gamma} = \frac{1}{\gamma \sigma_{Cal}} \quad C_{Bulk} = \epsilon_{rel} \epsilon_0 \frac{a^2}{a} = \epsilon_{rel} \epsilon_0 \gamma \quad (2)$$

where  $\epsilon_0 = 8.85 \cdot 10^{-12}$  F/m and  $\gamma = a^2/a = a$  indicating the permittivity of vacuum and the cell constant (electrode-geometry factor), respectively. These parameters determine the so-called Maxwell-Wagner frequency,  $f_{MW}$ , which is an inherent property of each aqueous medium:

$$f_{MW} = \frac{1}{2\pi R_{Bulk} C_{Bulk}} = \frac{\sigma_{Cal}}{2\pi \epsilon_{rel} \epsilon_0} \quad (3)$$

For the calibration solution with a conductivity of  $\sigma_{Cal} = 0.1307$  Sm $^{-1}$  and a relative permittivity of  $\epsilon_{rel} = 80$ , the Maxwell-Wagner frequency is approx. 29 MHz. This frequency would also be obtained from  $R_{Bulk}$ ,  $C_{Bulk}$  and the generalized cell constant  $\gamma$ . Nevertheless, from the semicircles of the bipolar and unipolar electrodes in Figure 2A, characteristic frequencies of 825 kHz and 1.79 MHz were identified. The explanation of these experimental deviations requires higher capacitive contributions than predicted by equation (3) (see subsequent discussion).

### Cell constants of the DBS electrodes

#### Experimental determination of the cell constants

Because of the uncertainties in the capacitive contributions, we experimentally determined the cell

constants  $\gamma$  in [m] of the electrodes from their resistances. The resistances were derived from the impedance spectra of four unipolar and four bipolar electrodes in a calibration solution. The specific conductivity  $\sigma_{Cal} = 0.1307$  Sm $^{-1}$  of the calibration solution corresponds to  $\rho_{Cal} = 7.6511$   $\Omega$ m at 21.3 °C. It was cross-checked with a temperature-compensated conductometer (Seven2Go, Mettler Toledo GmbH, Gießen, Germany). In the calibration solution, the cell constant  $\gamma$  may be obtained from the resistance  $R_{Cal}$  and the specific conductivity  $\sigma_{Cal}$  [48]:

$$\gamma = \frac{1}{\sigma_{Cal} R_{Cal}} = \frac{\rho_{Cal}}{R_{Cal}} \quad (4)$$

To determine  $R_{Cal}$ , the CPE and bulk contributions must be separated in the impedance spectra. Thus, we used a phenomenological interpretation of the impedance spectra (Figure 2A). While the low frequency CPE part of the measuring data enabled a linear regression, the high frequency (bulk) part could be fitted by a semicircle [26, 49]. Matlab was used for fitting. The overall impedance of the electrode results from the series connection of the two contributions that can be obtained from equations (1) and (2) (Figure 2C). Accordingly, extrapolations of the straight line towards high frequencies and the semicircle towards low frequencies provide the same point on the abscissa, which corresponds to the electrode resistance  $R_{Cal}$  (Figure 2A).

With the cell constants, the  $R_{Bulk}$  data of the animal models may be recalculated into effective specific resistivities:

$$\rho_{Bulk} = \gamma R_{Bulk} \quad (5)$$

$\rho_{Bulk}$  represents integrative tissue parameters with time-dependent contributions of the free interstitial fluid, adventitia, and neuronal tissue. Of the two methods for the extrapolation of  $R_{Bulk}$  from the complex plot, we prefer fitting of the straight branch (Figure 2A). We believe that this approach ensures a better comparability of the calibration with the *in vivo* tissue data. The main reason is the complicated frequency dependence of the *in vivo* impedance in the semicircle range. This is caused by the dielectric structure of the brain tissue, which introduces additional dispersion processes and a deformation of the semicircle (cf. subsequent experimental spectra).

#### Numerical calculations

The numerical calculations were conducted with the finite-element-software Comsol Multiphysics® 5.0. To calculate the cell constants and the field distributions, the electric current module and a stationary solver were used. For both electrode types, meshes with approx. 5 million mesh elements (the sum of the domain, boundary, and edge elements) were created. The same mesh geometries were used for the unipolar and bipolar electrodes (Figure 3). Around the electrode tips, spherical volumes of 2-mm diameters were fine-meshed with 4,019,287 (unipolar) and 4,652,039 (bipolar) domain elements, respectively. These volumes were enveloped by spherical volumes of an 80-mm diameter with cruder meshes of 832,224 (unipolar) and 496,124 (bipolar) domain elements. The high number of mesh elements for the unipolar electrode was generated because of the separated counter-electrode. It comprised a 30-mm long conducting cylinder assumed to protrude rectangular from the unipolar electrode with a diagonal distance of 3 mm to its base (Figure 3A). In the rat, the implanted counter electrode comprised a 30 mm long, 200- $\mu$ m gold wire. Its distance to the stimulation electrode shaft scattered at approximately 3 mm, depending on the implanting details and the geometry of the rat skull.

The domain properties were set to the properties of the calibration solution with a conductivity of 0.1307  $\text{Sm}^{-1}$  and a relative permittivity of 80. The electrode currents were set to 200  $\mu\text{A}$ , and the counter electrodes were set to ground. The outermost sphere boundaries were set to “electric insulation”. For a crosscheck with the experimental results, the cell constants were numerically calculated using equation (4) for  $R_{Cal} = U_{el}/I_{el}$ , with  $U_{el}$  and  $I_{el}$  and comprising the voltage and the current at the electrode tip surface, respectively.

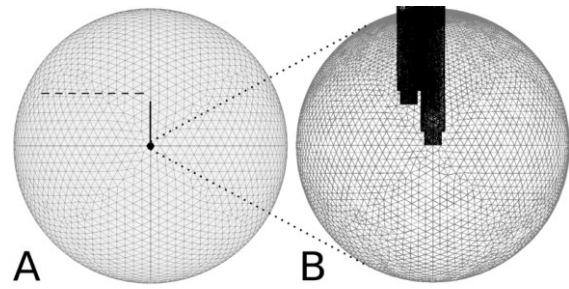


Figure 3: Schemes illustrating the geometries used in the finite-element simulations of the unipolar and bipolar electrodes. (A) Locations of the electrodes (vertical line) and the counter electrode of the unipolar electrode (dashed). (B) Locations of the electrode tips in the central, spherical domain with the finer mesh. The diameters of the outer and inner spherical domains were 80 and 2 mm, respectively.

#### Animals

Male Wistar Han rats (240 - 260 g) were obtained from Charles River Laboratory, Sulzfeld, Germany and housed under temperature-controlled conditions in a 12 h light-dark cycle with conventional rodent chow and water provided *ad libitum*. The study was conducted in accordance with the European Community Council directive 86/609/EEC for the care of laboratory animals and was approved by the local Animal Care Committee (LALLF M-V/TSEM/7221.3-1.2-019/10).

#### Electrode implantation

For electrode implantation, naive rats were anesthetized by intraperitoneal application of ketamine hydrochloride (10 mg per 100 g body weight, Ketanest S®, Pfizer, Karlsruhe, Germany) and xylazine (0.5 mg per 100 g body weight, Rompun®, Pfizer). The eyes were protected from dehydration using Vidisic® (Bausch and Lomb, Berlin, Germany). The surgical procedure was performed using a stereotactic frame (Stoelting, Wood Dale, IL, USA). The skull was opened by a dental rose-head bur (Kaniedenta, Herford, Germany) prior to electrode implantation into the right hemisphere. The stimulating tips of the electrodes were localized in the subthalamic nucleus (STN), which comprises one of the most important target regions for the treatment of PD in humans. The tip coordinates relative to bregma were: anterior-posterior (AP) = -3.5 mm, medial-lateral (ML) = 2.4 mm and dorsal-ventral (DV) = -7.6 mm (Paxinos and Watson, 2007). The electrodes were fixed to the skull by an adhesive-glyc bridge of dental acrylic (Pontiform automix 10:1, Müller & Weygandt GmbH, Bidingen, Germany), including an anchor screw that was tightened to the skull on the left hemisphere. Figure 4 illustrates the unipolar electrode model.

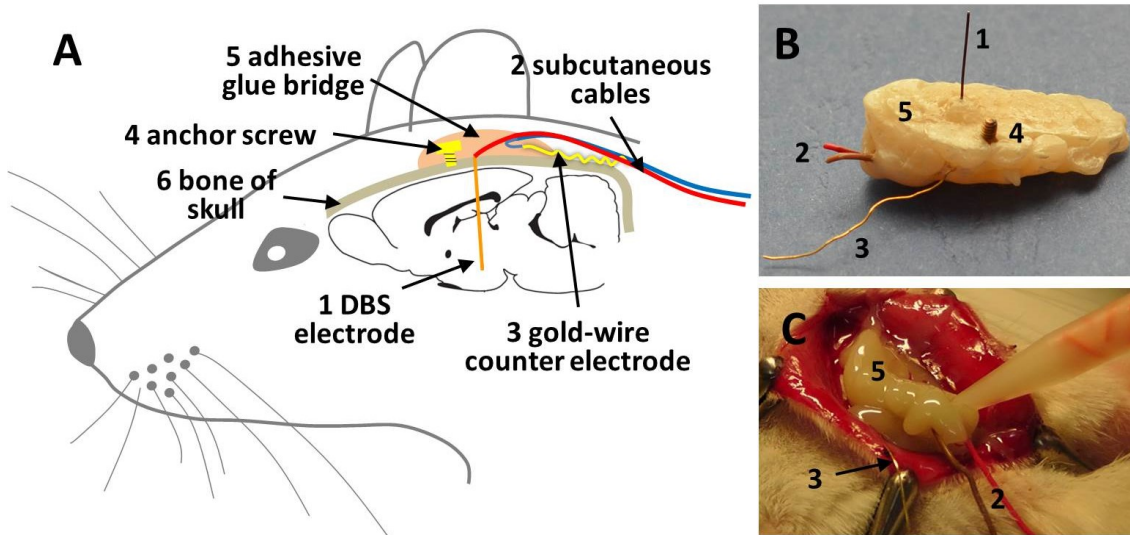


Figure 4: Implanted unipolar DBS electrode with gold-wire counter electrode. (A) Scheme of a sectional plane through the skull with: (1) unipolar Pt/Ir electrode, (2) connecting cables of stimulating and counter electrode, (3) gold-wire counter electrode, and (4) anchor-screw that was tightened to the skull on the left hemisphere. All components were embedded in an adhesive-glue bridge of biocompatible dental acrylic (5) that fixed the mounting to the skull. (B) Explanted DBS mounting. (C) Details of the surgical treatment. The operational area is spread by surgical clips. The connecting cables of the stimulating and counter electrodes are covered with biocompatible dental acrylic.

Following electrode implantation, the cables of the stimulating and counter electrode contacts were subcutaneously implanted with a central dorsal outlet port. After surgery, the wound was sutured, and the rats received 0.1 ml novaminsulfone (Ratiopharm, Ulm, Germany) and 4 ml saline subcutaneously. To prevent hypothermia, the rats were exposed to red light until the normalization of vital functions.

#### Chronic instrumentation

For chronic instrumentation, a plug connector was crimped to the cables of the DBS electrodes one week after electrode implantation. The connector ensured flexibility in the use of the commercial rat jackets (Lomir

Biomedical, Quebec, Canada), which contained the stimulators and batteries in a custom-made textile backpack. The miniaturized DBS stimulators had a PMMA housing and a 12-V battery for the constant current source of the stimulator. For details, see [22].

#### Impedance of the implanted electrodes

The rats received a unipolar electrode with a gold-wire counter electrode or a bipolar electrode with parallel shifted tips (Table 1). The same stimulators were used for both electrode types. Impedance measurements were conducted daily for approx. 12 minutes. For measurements, the rats were anesthetized with ketamine/xylazine.

Table 1: Experimental *in vivo* conditions

	Bipolar electrode	Unipolar electrode
Animal-group size	4	9
Counter electrode	Intracerebral shorter electrode	Subcutaneous gold wire (Figure 4)
Stimulating signal	60 $\mu$ s rectangular constant current (200 $\mu$ A negative) pulses of 130 Hz repetition rate; capacitive compensation current between the pulses	

## Results

### Additional capacitance contributions to the electrode properties

For an ideal electrode, the same cell constant would apply for the  $R_{Bulk}$  and  $C_{Bulk}$  values obtained from the conductivity and permittivity of the immersing medium (equation (2)). Accordingly, the  $R_{Bulk}-C_{Bulk}$  time constant in Figure 2 with  $R_{Bulk} = R_{Cal}$  and  $C_{Bulk} = C_{Cal}$  should correspond to the Maxwell-Wagner frequency of the calibration

solution according to equation (3) (refer to Table 2 for parameters). Nevertheless, to explain the time constants of the semicircles in Figure 2A, higher electrode resistances or additional electrode capacitances ( $C_{Add}$ ) that were significantly increased compared with the bared electrode tips (Table 2) had to be assumed for both electrode types. ( $C_{Add}$ ) were approx. 10.5 pF and 10.9 pF for the unipolar and bipolar electrodes, respectively. In tests with water, alcohol and air, these capacitances were

changed consistently with the different permittivities of the media (results not shown).

Clearly, the largest contribution to ( $C_{Add}$ ) stemmed from the immersed parts of the electrode shafts in aqueous solution (Figure 2C). Reasonable estimates for the shaft capacitances were obtained from the effective areas of the electrode insulations. These areas were estimated with the assumptions of open cylinders located in the central plains of the insulations with diameters of 225 (unipolar) and 150  $\mu\text{m}$  (bipolar) (cf. Figure 1). In the estimation of the shaft capacitances, we assumed mean immersion depths of the electrodes of 90%, an insulation thickness of 25  $\mu\text{m}$ , and a relative permittivity of 3 for the polyesterimide insulation [51].

For the unipolar electrode, a shaft capacitance of approx. 8.7 pF was obtained. This is slightly below the required ( $C_{Add}$ ) of approx. 10.9 pF likely because the stray capacitances of the measuring beaker and the external wiring were not taken into account. For the bipolar electrode, geometrical capacitance estimations are not easy. Applying the previously described estimations to the two parallel wires, capacitances of approx. 5.7 pF were obtained for each wire insulation. Nevertheless, the capacitances cannot simply be summed because they are switched in series with respect to their metal cores. We suggest that stray capacitances across the measuring beaker, between the individual wires and the shielding of the impedance device, play a role for each wire. This

finding, together with the external wiring likely led to the obtained ( $C_{Add}$ ) of approx. 10.5 pF.

Other sources of experimental deviations include differences in the immersion depth of the electrodes, as well as uncertainties in the wiring of the measuring setup, the uneven thickness of the insulation layers and the areas of the bared electrode tips. We suggest that a general understanding of the capacitive electrode properties is important for a correct picture. Thus, it should be noted that the capacitive electrode environment and the wiring conditions are different in the animal experiments. In this manuscript, an exact quantitative interpretation of the capacitive electrode properties is not required for parameter interpretation (see discussion).

*Electrode properties: experimental and numerical cell constants*

We demonstrated that  $R_{Bulk}=R_{Cal}$  correctly reflects the cell constant of the bared electrode tips and the resistivity of the calibration solution. The reason is that resistive currents require galvanic contact between the electrolytic solution and the electrode metal, which is present only at the bared electrode tips. Table 2 summarizes the experimental and numerical results. The good agreement between the experimental and numerical cell constants demonstrates the applicability of our approach.

Table 2: Comparison of experimentally obtained parameters in calibration solution with numerical cell constants. The capacitances that correspond to  $R_{cal}$  were calculated from the experimental cell constants with equation (2).

Electrode	Measurements			Corresponding capacitance	Numerical results
	$R_{cal} \pm \text{SEM} [\Omega]$	$\sigma [\text{Sm}^{-1}]$	$\gamma \pm \text{SEM} [\mu\text{m}]$	$C_{cal} \pm \text{SEM} [\text{pF}]$	$\gamma [\mu\text{m}]$
bipolar	$17,544 \pm 1,933$	0.1307	$460 \pm 65$	$0.33 \pm 0.05$	418
unipolar	$7,631 \pm 78$	0.1307	$1049 \pm 13$	$0.74 \pm 0.01$	989

*Numerical results: field distributions*

Figure 5 illustrates simulated distributions of the electric field around both electrode types. Please note that the values were calculated with average mesh sizes of approx. 16  $\mu\text{m}$  (unipolar electrode) and 10  $\mu\text{m}$  (bipolar electrode). This size is of the order of the effective cell-soma size of approx. 10  $\mu\text{m}$ .

Field strength peaks were identified at the electrode tips and the edges of the passivations. For the two electrode types, maximum peaks of 33.9 kV/m (unipolar) and 78.2 kV/m (bipolar) appeared at the electrode front edges (pointing arrows in Figure 5). The factor of 2.3 between the field strength peaks corresponds to the quotients of the cell constants (cf. Table 2; quotient of experimental results: 2.28; quotient of numerical results: 2.37).

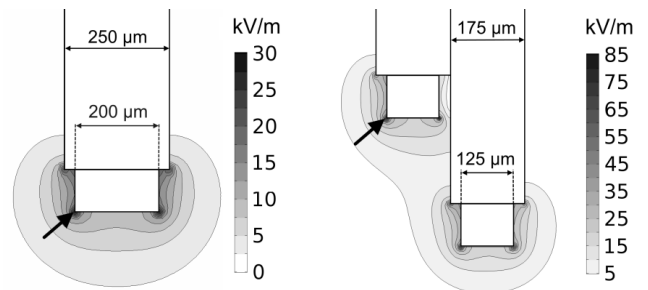


Figure 5: Numerical results of the field strength distributions in the central plane of the unipolar and bipolar electrodes. The 200  $\mu\text{A}$  constant-current setting at medium conductivities of 0.1307 S/m led to potentials of 1.56 V and 3.69 V against the counter electrode at ground potential (0 V) for the unipolar and bipolar electrodes, respectively. Please note that the distributions are not axially symmetric for the bipolar electrode.

**Impedance measurements in the brain**

Figure 6 presents impedance measurements with the bipolar electrodes in dependence on the day after implantation. Each of the plotted  $Real(Z^*)$  spectra was averaged over four electrodes of different animals. Despite the individual differences, the scatter is also a result of the low signal-to-noise-ratio caused by the low measuring voltage (12.5 mV<sub>PP</sub>). It was used to minimize current effects on the brain tissue.

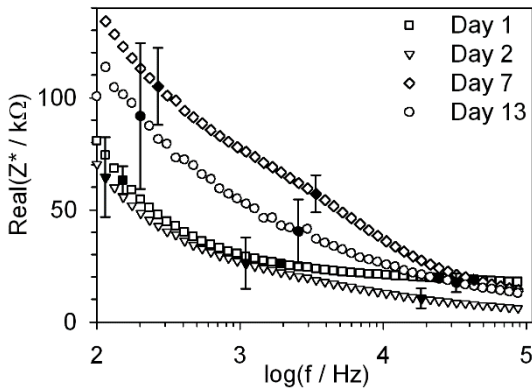


Figure 6: *In vivo* changes in  $Real(Z^*)$  for bipolar electrodes in the frequency range of 100 Hz to 100 kHz over 13 days. A characteristic decrease at the second day after implantation was identified in each of the four animals used in the experiments. For a clearer presentation, SEMs are only provided for the filled points as examples.

In the low frequency range of the spectra, the characteristic increase in the  $Real(Z^*)$  values for decreasing frequencies suggests the influence of electrode processes, which makes the extraction of tissue properties difficult [26, 52]. Below 14 kHz, a characteristic decrease in the  $Real(Z^*)$  spectra occurred at day two after implantation, followed by a systematic increase up to day seven. DBS was initiated at day eight and resulted in another impedance decrease at day 13.

At first glance, the relations were less clear when the raw data of the brain impedance were plotted in the complex plane. Figure 7 presents examples. Similar to the calibration solution, the high frequency branches reflect the bulk properties of the medium that surrounds the electrode. Nevertheless, the additional structural dispersions in the encapsulation tissue deformed the plots and flattened the semicircle branches [29]. Please compare Figure 2A (electrodes measured in calibration solution) with Figures 7A1 and 7B1 (electrodes measured in the brain).

In general, semicircles that span a larger abscissa range indicate an increased resistance of the encapsulation tissue. The slopes of the straight (“constant phase”) branches of the unipolar electrodes were reduced with time after implantation, whereas the slopes of the bipolar electrodes were rather stable (compare Figures 7A and B).

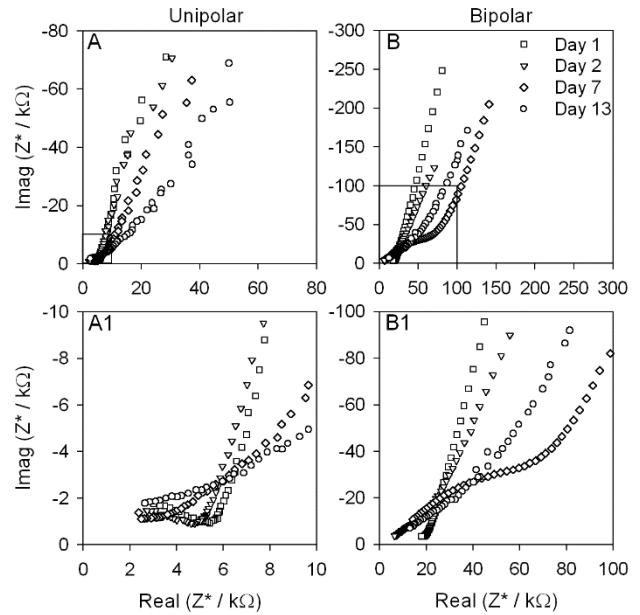


Figure 7: Complex plots of the impedances of unipolar (A, A1) and bipolar (B, B1) electrodes in dependence on the day after implantation. Each spectrum was measured in a frequency range of 100 Hz to 10 MHz. For clarity, not all measuring points were plotted. (A1) and (B1) are zooms of (A) and (B).

The interpretation of the daily measurements required a rigorous refinement of the large data numbers. In our straightforward approach, we derived the  $R_{Bulk}$  values by fitting the CPE branches (cf. Figure 2). The effective specific resistivities  $\rho_{Bulk}$  were calculated with equation (5) using the experimental cell constants of Table 2. In the calculations, the SEMs of the cell constants and the laws of error propagation were taken into account. Our data interpretation discriminated against fluctuations of single impedance values.

Figure 8 summarizes the resistivities of the bipolar and unipolar electrodes for two weeks after implantation. The resistivities of the brain tissue around the tips were similar for both electrode types and exhibited characteristic time-courses. Nevertheless, the mean resistivities of the bipolar electrodes changed within a substantially larger range (between approx. 2.2 and 28  $\Omega$ m) compared with the unipolar electrodes (between approx. 4.6 and 9.2  $\Omega$ m). Typically, the resistivities decreased at the second day after implantation, followed by an increase. The initiation of the DBS stimulation at day eight resulted in another resistivity decrease.

Figure 9 indicates the resistivity behavior of each of the bipolar electrodes summarized in Figure 8. The differences in the four individual DBS electrodes suggest that the ingrowth process may be individually traced.

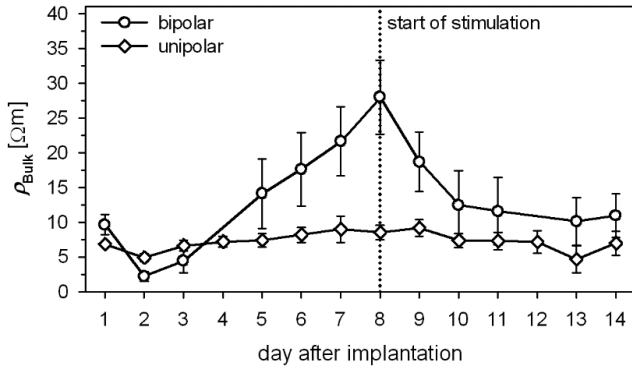


Figure 8: *In vivo* time courses of the effective specific resistivities of the brain tissue that surrounded four bipolar and nine unipolar electrodes (mean values  $\pm$  SEM). The vertical dotted line indicates the DBS initiation.

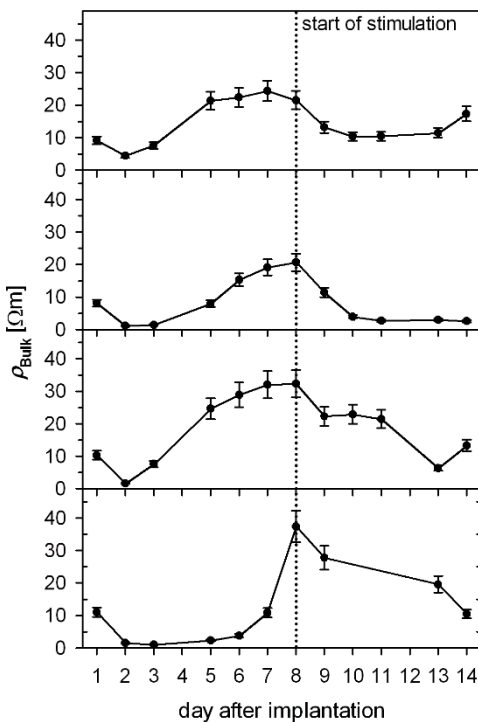


Figure 9: Individual plots of the four bipolar electrodes summarized in Figure 8. Despite the qualitatively similar pictures, the plots suggest a strongly individual behavior. Missing experimental points were caused by data-logging problems with the impedance setup.

## Discussion

### Pretests

Custom-made unipolar and bipolar Pt/Ir electrodes with polyesterimide insulated shafts enabled long-term experiments for more than six weeks [22]. The analysis of their physicochemical properties and impedance spectra led to the idea of registering changes in the effective specific resistivity of the medium around the bared electrode tips to trace the ingrowth process in the rat brain.

In previous experiments with the unipolar setup, we tested different counter electrodes, which were pierced

into the neck skin of rats [34]. The counter electrodes comprised dental wire rings composed of biocompatible, nickel-free steel alloy or arrays of small suture clips. The arrays were also used to detect “pure” counter electrode effects between pairs of clips and enabled the impedance changes to be monitored during the ingrowth process. We determined that the tested counter electrodes, their position, shape or material did not influence the impedance of the unipolar electrode (results not published). In the experiments, we also tested the gold-wire electrode used in the current study. Its advantages included the chemical stability, biocompatibility and ease of handling because it did not require additional surgical measures (compare with Figure 4C).

### How are cell constants expressed in electrode impedance spectra?

At first glance, the complex plots of the impedance data in the calibration solution appeared typical for bare metal electrodes (Figure 2). The constant phase behavior reflected the electrode polarization processes at low frequencies, whereas the semicircles indicated the resistor-capacitor (RC) behavior of the bulk medium at frequencies beyond the cessation of electrode polarization. The  $R_{Bulk}$  resistances (Figure 2) reflect ionic currents in the bulk medium, which is in galvanic contact with the bared electrode tips. In the calibration solution, the resistances  $R_{Cal} = R_{Bulk}$  are given by equation (2) or (5) using the conductivity and cell constants (Table 2). The corresponding capacitances ( $C_{Bulk}$ ) obtained from the medium permittivity and the cell constants (equation (2), Table 2) were superseded by  $C_{Add}$  in the measuring setup as demonstrated by the high capacitances required to explain the characteristic frequencies of the semicircles (Figure 2A). These frequencies were substantially lower than the Maxwell-Wagner dispersion frequency of the calibration solution of approx. 29 MHz. Nevertheless, the diameters and shapes of the semicircles, as well as the DC and low frequency behavior of the electrodes are not altered by  $C_{Add}$ . In the calibration solution, geometric fits of the two branches by a straight line and a semicircle merge at the real axis, which provides the same resistances  $R_{Cal} = R_{Bulk}$ .

This behavior is inherent to our circuit model, which effectively consists of the CPE in series with a parallel RC pair (Figure 2C). Beyond the CPE dispersion at high frequencies (equation (1)), the extrapolated merging point at the real axis is defined by  $R_{Bulk}$ . For the behavior of the circuit, it is unimportant which of the CPE poles  $C_{Add}$  is connected to because significant capacitive current across the electrode insulation flows only at frequencies where potential electrolytic processes at the insulation surface have previously dispersed by capacitive CPE bridging.

### Determination of cell constants

For the experimental and numerical determinations of the cell constants, the specific conductivity of 0.1307 S/m of the calibration solution was used. This conductivity corresponds with human grey matter at 65 kHz. At the basic frequency of the DBS signal of 130 Hz, its conductivity is 0.0915 S/m and increases with frequency [53]. Sixty-five kHz corresponds to the 500<sup>th</sup> harmonic frequency of the 130-Hz DBS pulse. Taking into account all harmonic frequencies up to 65 kHz ensures a good fidelity of the pulse shape [26]. This frequency is sufficiently high to prevent electrode processes from influencing the experiments (Figure 2A), whereas wiring inductances and capacitances may be neglected in the experimental determination of the cell constants (Figure 2B), as well as in animal experiments.

For the results of the finite-element simulations, the domain geometries around the electrodes were important. For the bipolar electrode, the domain geometries did not impose a problem because the current source and current drain were both located in the center of the calculation space with vanishing current contributions in the periphery. In contrast, the results for the unipolar electrode sensitively depended on the location and geometry of the counter electrode. Experimental resistances or cell constants were useful parameters to test the applicability of the geometry chosen for the numerical model.

For example, the numerically calculated resistance for the unipolar electrode with a spherical counter electrode at an infinite distance was only 82.8% of the resistance obtained with the cylindrical counter-electrode (dashed in Figure 3A). Using the infinitely distant spherical counter electrode as a reference for a hypothetical spherical "equivalent electrode", a diameter of 188.9  $\mu\text{m}$  was analytically calculated [48]. Neglecting electrode processes, this equivalent electrode has the resistance of the unipolar electrode and the same voltage-current behavior. At larger distances, it generates the same field distribution as the actual electrode. Equivalent electrodes enable intuitive considerations of all relevant parameters. We used these considerations to confirm that our stimulators could provide sufficient voltage for the adjusted current at the given tissue impedances.

### Characteristic properties of the CPE branches

In the impedance measurements, the same voltages were used for all electrodes. In the calibration solution, the CPE slope-exponents were  $\alpha=0.73$  and  $\alpha=0.78$  for the fresh bipolar and unipolar electrodes, respectively (Figure 2). Exponents closer to unity reflect increased capacitive currents and reduced conductive (Ohmic) currents, which are mediated by electric double layer processes. The slightly increased conductive contributions for the bipolar

electrode are likely caused by the increased local current densities at electrode sites with increased curvature. An overall increased curvature results from the increased edge-to-plain-surface ratio of the bipolar electrode (cf., for example, to the characteristic V-I curves of the electrode in [26]). The increased current densities in the immediate vicinity of the metal contacts result in increased contributions to the overall resistivity compared with the unipolar electrode. This is one reason for the increased sensitivity of the bipolar electrode for the surrounding medium properties.

For the unipolar electrode, the contribution of the counter electrode to the impedance may be neglected throughout the frequency-measuring range. The reason is its very large surface area, which results in high capacitive and low conductive current densities. Accordingly, the CPE impedance of the unipolar electrode (Figure 2) is solely generated by currents that pass through the double layer at a single tip, whereas the CPE impedance of the bipolar electrode is generated at two tips switched in series.

Calculations with equation (1) demonstrated that two CPEs of equal electrical properties in series exhibit the same slope in the complex plane as the single CPE. The halved effective capacitance shifts the location of the frequency points at the CPE plot upwards (Figure 2A). As a result, the CPE effects are pronounced in a wider frequency range of the spectrum. This is another reason for the increased sensitivity of the bipolar electrode for the surrounding medium properties. Moreover, in our experiments, CPE fitting was facilitated because more measuring points were located further away from the frequency range of the interference with the structural dispersions.

### Influence of additional capacitances on the electrode impedance

The medium capacitances at the bared electrode tips in the control measurements were superimposed with additional shaft and wiring capacitances (Table 2). In the animal model, these additional capacitances are likely increased because of the complete "immersion" of the electrodes and the subcutaneous wiring. An exact analysis was hindered by the structural dispersions of the brain tissue, which deformed the semicircle branch in the animal experiments.

There are two additional things that must be considered: i)  $C_{Add}$  introduce low-pass filter characteristics for the electrode wiring. This will not lead to distortions of the DBS needle pulse-shape as long as the cut-off frequency is greater than 1 MHz, i.e., the highest significant harmonic frequencies of the signal (cf. to [26] for the Fourier content of the DBS signal). For our setup, this condition was roughly fulfilled. ii) The electrical

double layer effects at the insulation-medium interface should not contribute to the CPE properties. This condition was fulfilled because significant currents across this interface require the capacitive bridging of the insulation. At the high frequencies required for bridging, electrical double layer effects may be neglected (compare area specific capacitances of the electric double layer and the insulation layer).

#### *Resistivity detection in the brain*

In the animal model, the deformation and flattening of the semicircle by structural dispersions of the brain tissue in the frequency range of the  $\beta$ -dispersion resulted in a vertical shift of its center [29]. As a result, fitting the intercepts of the semicircles with the real axis became impossible (compare with Figure 7). The fits of the linear CPE branches provided reasonable results, which we interpret as the effective resistivities of the brain tissue that surrounds the electrode tip (Figure 8). To discriminate against the influence of the structural dispersions, we neglected measuring points in the transition ranges between the linear and semicircle branches in the fits.

The detected resistivity changes were qualitatively similar for both electrode types; however, they were substantially more pronounced for the bipolar electrodes (Figure 8). A characteristic decrease at the second day was followed by a successive increase in the electrode resistivity at an individual pace from the third day on (Figure 9). These findings are consistent with the findings of [33]. These authors ascribed the impedance increase of a unipolar electrode in the brain of a rhesus macaque to the foreign body reaction, which was accompanied by the formation of the adventitia. The authors left the impedance decrease one day after implantation, which is visible in their figure 4B, uncommented. We suggest that these drops are characteristic and caused by the influx of wound fluid into the electrode-tissue interface [34]. [33] also described a stimulation-on-induced decrease in the electrode impedance, which stabilized in their experiments approximately five weeks post implantation. In our experiments, starting the continuous stimulation after eight days induced a resistivity decrease, followed by stabilization over the following days of stimulation.

The thickness of the adventitia that ultimately encapsulates the DBS electrodes is correlated with the intensity of the foreign body reaction [54]. Without a stimulating signal, the intensity of the reaction depends on the electrode material [38]. Adventitia formation is also influenced by the presence of the stimulating signal [41] likely because electrochemical reactions at the surface of stimulated electrodes alter their effective properties as “foreign bodies”.

#### *Numerical results on field distributions*

In the model, the edges of the electrodes were assumed to form perfect 90°-angles between the cylindrical flanks and the bottoms of the electrode tips (Figure 3). Microscopic investigations of the electrodes indicated rounded edges (Figure 1). Rounding leads to lower field strengths near the edges compared with our simulation results. For future setups, it is desirable to have electrodes with edges of defined curvatures. This approach will enable the improvement of model precision and the generation of better-defined fields in the brain.

The homogeneous electrical tissue properties assumed in the simulations correspond to a random orientation of the neuronal cells, which is abstracted from their dielectric structure. These structures introduce the complex frequency dependent properties of tissues and cell suspensions [55], which were ignored for simplicity. Our parameters avoided field strengths at sites of high electrode curvature that may have caused membrane poration and cell destruction. The relations are discussed in [5].

#### *Bipolar vs. unipolar electrodes*

Because of the smaller electrode geometries, in general, increased current densities occur in animal experiments compared with patients. In the experiments, we used the same current magnitude for both electrode types. Given their different cell constants, this approach led to stimulation voltages that were approximately twice as high for the bipolar electrode compared with the unipolar electrode (Figure 5). The increased electrode voltage resulted in increased field strengths and current densities at the surface of the bipolar electrode because these parameters are proportional to the electrode voltage [48]. Nevertheless, the field decays over shorter distances from the smaller tips of this electrode (Figure 5). For the bipolar electrodes, the surface voltage of the unipolar electrodes would be reached at constant currents of approx. 100  $\mu$ A because of the factor-of-two higher resistance. Although this would reduce the power consumption for the stimulator, it would reduce the reach inside the brain even further [5].

Despite the electrode tip geometries, models that are more realistic must consider the rat skull geometry, counter-electrode location, and inhomogeneous and frequency-dependent tissue properties to improve the simulation of the V-I dependence, the field distributions and the DBS effects in the rat brain.

#### *Conclusion and Outlook*

Here, we focus on the technical aspects of our comparative long-term *in vivo* DBS study with unipolar and bipolar electrodes in a rat model. At our current state of knowledge, we propose to use unipolar electrodes in

long-term behavioral studies with animals. These studies are important for a comparison with the clinical situation, in which unipolar stimulation is the preferred mode in PD patients. Our experiments for up to six weeks demonstrated greater beneficial effects for unipolar compared with bipolar DBS [22]. Unipolar stimulation has also been suggested for the hemiparkinsonian rat model by [17].

In animals, impedance registration may contribute to a better understanding of the ingrowth and encapsulation processes of electrodes, which are important for the adjustment of the stimulation parameters. There is likely more information in each impedance spectrum than the specific resistivity values obtained by linear fits of the low-frequency constant-phase branches; however, the approach is advantageous over recording the 1-kHz impedances of the electrodes [35]. It enabled us to monitor the individual ingrowth process.

The increased sensitivity of bipolar electrodes for resistivity changes in the surrounding tissue suggests the operation of bipolar electrodes in different modes, including the unipolar mode during stimulation and the bipolar mode in the impedance-registration of the ingrowth process. The integration of an impedance-detection mode into DBS stimulators for animals appears feasible. The obtained information may subsequently be used for a “knowledge-based” readjustment of the stimulation parameters.

Our methodology of extracting the specific resistivity from the impedance spectra of electrodes is also most likely suitable for the quantitative characterization of processes, such as the integration of medical implants. We suppose that not only the integration but also the loosening of formerly well-integrated implants will be reflected in the specific resistivities or conductivities of the surrounding tissue. These parameters may be obtained from the impedance of auxiliary contacts on the implants. It will be worthwhile to investigate whether biofilm formation and inflammation processes on implant surfaces or permanent catheters may be detected.

### Acknowledgments

The authors wish to thank R. Modrozynski for assistance with the microscopic electrode documentation, Prof. U. Gimsa for fruitful discussions on theoretical matters, our keeper G. Brüsck for animal care and Prof. R. Benecke for providing us with the possibility to use the animal laboratory of the Clinic of Neurology of the University of Rostock. Dr. K. Badstübner is grateful for a scholarship from the German Research Foundation (DFG, Research Training Group 1505/1 “welisa”). T. Kröger acknowledges financing by a project of the Federal Ministry of Economics and Technology (BMW, V230-630-08-TVMV-S-031). Part of the work was conducted within a project

financed by the Federal Ministry of Education and Research (BMBF, FKZ 01EZ0911). The custom-made stimulator system was developed in cooperation with the Steinbeis company (STZ1050, Rostock, Germany) and Dr. R. Arndt (Rückmann & Arndt, Berlin, Germany).

### References

1. Krack P, Hariz MI, Baunez C, Guridi J, Obeso JA. Deep brain stimulation: from neurology to psychiatry? *Trends Neurosci*. 2010;33:474-84. <https://doi.org/10.1016/j.tins.2010.07.002>
2. Weaver FM, Follett K, Stern M, Hur K, Harris C, Marks WJ, Jr., et al. Bilateral deep brain stimulation vs best medical therapy for patients with advanced Parkinson disease: a randomized controlled trial. *Jama*. 2009;301:63-73. <https://doi.org/10.1001/jama.2008.929>
3. Moro E, Lozano AM, Pollak P, Agid Y, Rehnrcrona S, Volkmann J, et al. Long-term results of a multicenter study on subthalamic and pallidal stimulation in Parkinson's disease. *Mov Disord*. 2010;25:578-86. <https://doi.org/10.1002/mds.22735>
4. Pizzolato G, Mandat T. Deep brain stimulation for movement disorders. *Front Integr Neurosci*. 2012;6:2. <https://doi.org/10.3389/fnint.2012.00002>
5. Gimsa U, Schreiber U, Habel B, Flehr J, van Rienen U, Gimsa J. Matching geometry and stimulation parameters of electrodes for deep brain stimulation experiments--numerical considerations. *J Neurosci Methods*. 2006;150:212-27. <https://doi.org/10.1016/j.jneumeth.2005.06.013>
6. Cheung T, Tagliati M. Deep brain stimulation: can we do it better? *Clin Neurophysiol*. 2010;121:1979-80. <https://doi.org/10.1016/j.clinph.2010.05.024>
7. Okun MS, Gallo BV, Mandybur G, Jagid J, Foote KD, Revilla FJ, et al. Subthalamic deep brain stimulation with a constant-current device in Parkinson's disease: an open-label randomised controlled trial. *Lancet Neurol*. 2012;11:140-9. [https://doi.org/10.1016/S1474-4422\(11\)70308-8](https://doi.org/10.1016/S1474-4422(11)70308-8)
8. Gross RE, McDougal ME. Technological advances in the surgical treatment of movement disorders. *Curr Neurol Neurosci Rep*. 2013;13:371. <https://doi.org/10.1007/s11910-013-0371-2>
9. Lettieri C, Rinaldo S, Devigili G, Pisa F, Mucchiut M, Belgrado E, et al. Clinical outcome of deep brain stimulation for dystonia: constant-current or constant-voltage stimulation? A non-randomized study. *Eur J Neurol*. 2015;22:919-26. <https://doi.org/10.1111/ene.12515>
10. Benazzouz A, Gao DM, Ni ZG, Piallat B, Bouali-Benazzouz R, Benabid AL. Effect of high-frequency stimulation of the subthalamic nucleus on the neuronal activities of the substantia nigra pars reticulata and ventrolateral nucleus of the thalamus in the rat. *Neurosci*. 2000;99:289-95. [https://doi.org/10.1016/S0306-4522\(00\)00199-8](https://doi.org/10.1016/S0306-4522(00)00199-8)
11. Salin P, Manrique C, Forni C, Kerkerian-Le Goff L. High-frequency stimulation of the subthalamic nucleus selectively reverses dopamine denervation-induced cellular defects in the output structures of the basal ganglia in the rat. *J Neurosci*. 2002;22:5137-48.

12. Bruet N, Windels F, Carcenac C, Feuerstein C, Bertrand A, Poupard A, et al. Neurochemical mechanisms induced by high frequency stimulation of the subthalamic nucleus: increase of extracellular striatal glutamate and GABA in normal and hemiparkinsonian rats. *J Neuropathol Exp Neurol*. 2003;62:1228-40.  
<https://doi.org/10.1093/jnen/62.12.1228>
13. Windels F, Carcenac C, Poupard A, Savasta M. Pallidal origin of GABA release within the substantia nigra pars reticulata during high-frequency stimulation of the subthalamic nucleus. *J Neurosci*. 2005;25:5079-86.  
<https://doi.org/10.1523/JNEUROSCI.0360-05.2005>
14. Boulet S, Lacombe E, Carcenac C, Feuerstein C, Sgambato-Faure V, Poupard A, et al. Subthalamic stimulation-induced forelimb dyskinesias are linked to an increase in glutamate levels in the substantia nigra pars reticulata. *J Neurosci*. 2006;26:10768-76.  
<https://doi.org/10.1523/JNEUROSCI.3065-06.2006>
15. Schulte T, Brecht S, Herdegen T, Illert M, Mehdorn HM, Hamel W. Induction of immediate early gene expression by high-frequency stimulation of the subthalamic nucleus in rats. *Neurosci*. 2006;138:1377-85.  
<https://doi.org/10.1016/j.neuroscience.2005.12.034>
16. Fang X, Sugiyama K, Akamine S, Namba H. Improvements in motor behavioral tests during deep brain stimulation of the subthalamic nucleus in rats with different degrees of unilateral parkinsonism. *Brain research*. 2006;1120:202-10.  
<https://doi.org/10.1016/j.brainres.2006.08.073>
17. So RQ, McConnell GC, August AT, Grill WM. Characterizing effects of subthalamic nucleus deep brain stimulation on methamphetamine-induced circling behavior in hemiparkinsonian rats. *IEEE Trans Neural Syst Rehabil Eng*. 2012;20:626-35.  
<https://doi.org/10.1109/TNSRE.2012.2197761>
18. Cooperrider J, Furmaga H, Plow E. Chronic deep cerebellar stimulation promotes long-term potentiation, microstructural plasticity, and reorganization of perilesional cortical representation in a rodent model. *J Neurosci*. 2014;34:9040-50.  
<https://doi.org/10.1523/JNEUROSCI.0953-14.2014>
19. Liu HY, Jin J, Tang JS, Sun WX, Jia H, Yang XP, et al. Chronic deep brain stimulation in the rat nucleus accumbens and its effect on morphine reinforcement. *Addiction biology*. 2008;13:40-6.  
<https://doi.org/10.1111/j.1369-1600.2007.00088.x>
20. Forni C, Mainard O, Melon C, Goguenheim D, Kerkerian-Le Goff L, Salin P. Portable microstimulator for chronic deep brain stimulation in freely moving rats. *J Neurosci Methods*. 2012;209:50-7.  
<https://doi.org/10.1016/j.jneumeth.2012.05.027>
21. Harnack D, Meissner W, Paulat R, Hilgenfeld H, Müller WD, Winter C, Morgenstern R, Kupsch A. 2008. Continuous high-frequency stimulation in freely moving rats: development of an implantable microstimulation system. *J Neurosci Methods* 2008;167:278-291  
<https://doi.org/10.1016/j.jneumeth.2007.08.019>
22. Badstuebner K, Gimsa U, Weber I, Tuchscherer A, Gimsa J. Deep brain stimulation of hemiparkinsonian rats with unipolar and bipolar electrodes for up to 6 weeks – behavioral testing of freely moving animals. *Parkinson's Dis*. 2017. (In press).
23. Ewing SG, Porr B, Riddell J, Winter C, Grace AA. SaBer DBS: a fully programmable, rechargeable, bilateral, charge-balanced preclinical microstimulator for long-term neural stimulation. *J Neurosci Methods*. 2013;213:228-35.  
<https://doi.org/10.1016/j.jneumeth.2012.12.008>
24. Spieles-Engemann AL, Collier TJ, Sortwell CE. A functionally relevant and long-term model of deep brain stimulation of the rat subthalamic nucleus: advantages and considerations. *European J Neurosci*. 2010;32:1092-9.  
<https://doi.org/10.1111/j.1460-9568.2010.07416.x>
25. Gubellini P, Kachidian P. Animal models of Parkinson's disease: An updated overview. *Revue neurologique*. 2015;171:750-61.  
<https://doi.org/10.1016/j.neurol.2015.07.011>
26. Gimsa J, Habel B, Schreiber U, van Rienen U, Strauss U, Gimsa U. Choosing electrodes for deep brain stimulation experiments—electrochemical considerations. *J Neurosci Methods*. 2005;142:251-65.  
<https://doi.org/10.1016/j.jneumeth.2004.09.001>
27. Herrington TM, Cheng JJ, Eskandar EN. Mechanisms of deep brain stimulation. *J Neurophys*. 2016;115:19-38.  
<https://doi.org/10.1152/jn.00281.2015>
28. Ungerstedt U. 6-Hydroxy-dopamine induced degeneration of central monoamine neurons. *Eur J Pharmacol*. 1968;5:107-10. [https://doi.org/10.1016/0014-2999\(68\)90164-7](https://doi.org/10.1016/0014-2999(68)90164-7)
29. Foster KR, Schwan HP. Dielectric properties of tissues. *Handbook of biological effects of electromagnetic fields*. 1995;2:25-102.
30. Kerner TE, Paulsen KD, Hartov A, Soho SK, Poplack SP. Electrical impedance spectroscopy of the breast: clinical imaging results in 26 subjects. *IEEE Trans Med Imaging*. 2002;21:638-45. <https://doi.org/10.1109/TMI.2002.800606>
31. Adler A, Amyot R, Guardo R, Bates JH, Berthiaume Y. Monitoring changes in lung air and liquid volumes with electrical impedance tomography. *J Appl Physiol*. 1997;83:1762-7.
32. Lueck S, Reichert D, Pliquett U, Minor T, Preusse CJ. Bioelectric impedance of the neonatal heart during normothermic ischemia. *Biomed Tech*. 2013;58: Suppl. 1, Walter de Gruyter. Berlin, Boston.  
<https://doi.org/10.1515/bmt-2013-4452>
33. Lempka SF, Miocinovic S, Johnson MD, Vitek JL, McIntyre CC. In vivo impedance spectroscopy of deep brain stimulation electrodes. *J Neural Eng*. 2009;6:046001.  
<https://doi.org/10.1088/1741-2560/6/4/046001>
34. Badstübner K, Kröger T, Mix E, Gimsa U, Benecke R, Gimsa J. Electrical impedance properties of deep brain stimulation electrodes during long-term in-vivo stimulation in the Parkinson model of the rat. In: Gabriel J, Schier J, Van Huffel S, Conchon E, Correia C, Fred A, et al., editors. *Biomedical Engineering Systems and Technologies*. Springer. 2013;357 ISBN:978-3-642-38255-0. pp. 287–97.

35. Williams JC, Hippensteel JA, Dilgen J, Shain W, Kipke DR. Complex impedance spectroscopy for monitoring tissue responses to inserted neural implants. *J Neural Eng*. 2007;4:410-23. <https://doi.org/10.1088/1741-2560/4/4/007>
36. Duan YY, Clark GM, Cowan RS. A study of intra-cochlear electrodes and tissue interface by electrochemical impedance methods in vivo. *Biomaterials*. 2004;25:3813-28. <https://doi.org/10.1016/j.biomaterials.2003.09.107>
37. Newbold C, Mergen S, Richardson R, Seligman P, Millard R, Cowan R, et al. Impedance changes in chronically implanted and stimulated cochlear implant electrodes. *Cochlear Implants Int*. 2014;15:191-9. <https://doi.org/10.1179/1754762813Y.0000000050>
38. Grill WM, Mortimer JT. Electrical properties of implant encapsulation tissue. *Ann Biomed Eng*. 1994;22:23-33. <https://doi.org/10.1007/BF02368219>
39. Otto KJ, Johnson MD, Kipke DR. Voltage pulses change neural interface properties and improve unit recordings with chronically implanted microelectrodes. *IEEE Trans Biomed Eng*. 2006;53:333-40. <https://doi.org/10.1109/TBME.2005.862530>
40. Charlet de Sauvage R, Lima da Costa D, Erre JP, Aran JM. Electrical and physiological changes during short-term and chronic electrical stimulation of the normal cochlea. *Hear. Res*. 1997;110:119-34. [https://doi.org/10.1016/S0378-5955\(97\)00066-X](https://doi.org/10.1016/S0378-5955(97)00066-X)
41. Lempka SF, Johnson MD, Moffitt MA, Otto KJ, Kipke DR, McIntyre CC. Theoretical analysis of intracortical microelectrode recordings. *J Neural Eng*. 2011;8:045006. <https://doi.org/10.1088/1741-2560/8/4/045006>
42. Abouzari MS, Berkemeier F, Schmitz G, Wilmer D. On the physical interpretation of constant phase elements. *Solid State Ionics*. 2009;180:922-7. <https://doi.org/10.1016/j.ssi.2009.04.002>
43. Jorcin J-B, Orazem ME, Pébère N, Tribollet B. CPE analysis by local electrochemical impedance spectroscopy. *Electrochimica Acta*. 2006;51:1473-9. <https://doi.org/10.1016/j.electacta.2005.02.128>
44. MacDonald JR. *Impedance Spectroscopy - Emphasizing Solid Materials and Systems*. Wiley. 1987:1-346.
45. Bisquert J, Garcia-Belmonte G, Bueno P, Longo E, Bulhoes L. Impedance of constant phase element (CPE)-blocked diffusion in film electrodes. *J Neuropathol Exp Neurol*. 1998;452:229-34. [https://doi.org/10.1016/S0022-0728\(98\)00115-6](https://doi.org/10.1016/S0022-0728(98)00115-6)
46. Conway BE, Bockris JO'M, White RE. *Modern Aspects of Electrochemistry*. Springer. 1999. ISBN:978-0306459641
47. Minnikanti S, Pereira MG, Jaraiedi S, Jackson K, Costa-Neto CM, Li Q, et al. In vivo electrochemical characterization and inflammatory response of multiwalled carbon nanotube-based electrodes in rat hippocampus. *J Neural Eng*. 2010;7:16002. <https://doi.org/10.1088/1741-2560/7/1/016002>
48. Nowak K, Mix E, Gimsa J, Strauss U, Sriperumbudur KK, Benecke R, et al. Optimizing a rodent model of Parkinson's disease for exploring the effects and mechanisms of deep brain stimulation. *Parkinson's Dis*. 2011;2011:414682.
49. Asami K. Characterization of heterogeneous systems by dielectric spectroscopy. *Progress in Polymer Science*. 2002;27:1617-59. [https://doi.org/10.1016/S0079-6700\(02\)00015-1](https://doi.org/10.1016/S0079-6700(02)00015-1)
50. Paxinos G, Watson C. *The Rat Brain in Stereotaxic Coordinates, Sixth Edition: Hard Cover Edition*. Academic Press. 2007. ISBN: 978-0125476126.
51. Ahmad Z. Polymeric dielectric materials, in *Dielectric Material*, ed. by Silaghi MA. InTech, Rijeka. 2012; 3-26.
52. Onaral B, Schwan H. Linear and nonlinear properties of platinum electrode polarisation. Part 1: frequency dependence at very low frequencies. *Medical and biological engineering and computing*. 1982;20:299-306. <https://doi.org/10.1007/BF02442796>
53. Gabriel S, Lau R, Gabriel C. The dielectric properties of biological tissues: II. Measurements in the frequency range 10 Hz to 20 GHz. *Phys Med Biol*. 1996;41:2251. <https://doi.org/10.1088/0031-9155/41/11/002>
54. Wintermantel E. *Medizintechnik mit biokompatiblen Werkstoffen und Verfahren*. Springer. 2002. ISBN:978-3540412618
55. Stubbe M, Gimsa J. Maxwell's mixing equation revisited: characteristic impedance equations for ellipsoidal cells. *Biophys. J*. 2015;109:194-208. <https://doi.org/10.1016/j.bpj.2015.06.021>